Research Article

Nano Research
2022, 15(1): 352–360

ISSN 1998-0124 CN 11-5974/O4
https://doi.org/10.1007/s12274-021-3482-0

Lithiophilic N-doped carbon bowls induced Li deposition in layered graphene film for advanced lithium metal batteries

Xiaoyu Feng[1,2,§], Hong-Hui Wu[3,§], Biao Gao[2], Michał Świętosławski[4], Xin He[5] (✉), and Qiaobao Zhang[1] (✉)

[1] *Department of Materials Science and Engineering, College of Materials, Xiamen University, Xiamen 361005, China*
[2] *The State Key Laboratory of Refractories and Metallurgy and Institute of Advanced Materials and Nanotechnology, Wuhan University of Science and Technology, Wuhan 430081, China*
[3] *School of Materials Science and Engineering, University of Science and Technology Beijing, Beijing 100083, China*
[4] *Faculty of Chemistry, Jagiellonian University, ul. Gronostajowa 2, 30-387 Krakow, Poland*
[5] *School of Chemical Engineering, Sichuan University, Chengdu 610065, China*
[§] *Xiaoyu Feng and Hong-Hui Wu contributed equally to this work.*

© Tsinghua University Press and Springer-Verlag GmbH Germany, part of Springer Nature 2021
Received: 15 February 2021 / **Revised:** 29 March 2021 / **Accepted:** 29 March 2021

ABSTRACT

Lithium (Li) metal with high theoretical capacity and low electrochemical potential is the most ideal anode for next-generation high-energy batteries. However, the practical implementation of Li anode has been hindered by dendritic growth and volume expansion during cycling, which results in low Coulombic efficiency (CE), short lifespan, and safety hazards. Here, we report a highly stable and dendrite-free Li metal anode by utilizing N-doped hollow porous bowl-like hard carbon/reduced graphene nanosheets (CB@rGO) hybrids as three-dimensional (3D) conductive and lithiophilic scaffold host. The lithiophilic carbon bowl (CB) mainly works as excellent guides during the Li plating process, whereas the rGO layer with high conductivity and mechanical stability maintains the integrity of the composite by confining the volume change in long-range order during cycling. Moreover, the local current density can be reduced due to the 3D conductive framework. Therefore, CB@rGO presents a low lithium metal nucleation overpotential of 18 mV, high CE of 98%, and stable cycling without obvious voltage fluctuation for over 600 cycles at a current density of 1 mA·cm^{-2}. Our study not only provides a good CB@rGO host and pre-Lithiated CB@rGO composite anode electrode, but also brings a new strategy of designing 3D electrodes for those active materials suffering from severe volume expansion.

KEYWORDS

dendrite inhibition, Li metal host, lithium metal battery, bowl-like carbon/reduced graphene nanosheets hybrids

1 Introduction

The ongoing development of batteries has made remarkable improvements in their applications, such as energy density, power density, and cycle life. With the continuous increase in the demands for electric vehicles and portable electronic devices from the current world, research on batteries, particularly for the aspect of higher energy density is highly desired [1–4]. Rechargeable lithium (Li) metal-based batteries (LMBs) are attracting increasing attention as high energy storage candidates, and have been extensively investigated for electrochemical energy storage devices [5–7]. However, the practical application of LMBs faces several challenges, including the low Coulombic efficiency, the growth of Li dendrites, and the large volume change during the electrochemical process [8–11]. Due to the highly reactive nature of Li metal, it reacts easily and spontaneously with organic electrolytes and forms solid electrolyte interphase (SEI) film. The uncontrollable growth of Li metal dendrite can continually expose fresh Li to electrolyte after the fracture of SEI [12, 13]. With the durative forming and continuous growth of the Li dendrites during repeated cycling, the constant consumption of active Li and electrolyte leads to low reversibility and short cycle life. In addition, the preference of Li stripping the root of Li dendrites can induce the formation of dead Li. The accumulation of dead Li accompanied by serious growth of Li dendrites could cause a dimension change, resulting in internal stress fluctuation and a floating interface in the cell. Moreover, the dendrites could potentially lead to an internal short circuit and a thermal runaway with safety hazards. Therefore, suppressing the uncontrolled growth of Li dendrites and governing the dimension change during the electrochemical process is considered to be critical for the practical utilization of Li metal anode [9, 14, 15].

Many strategies have been reported to effectively regulate the morphology of electrodeposited Li, such as, exploiting electrolyte additives for SEI modification [16–19], engineering stable artificial interfacial layer to facilitate Li-ions diffusion and inhibit Li dendrite growth [20–25], and constructing a three-dimensional (3D) host structure for Li metal [26–32]. Since the origin of the dendritic Li growth arises from the spatial inhomogeneity in charge distribution over the electrode surface. It is a clear advantage for the 3D host design comparing to other proposed strategies. The 3D host electrode could provide the framework with a large surface area for electrochemical

Address correspondence to Xin He, xinhe@scu.edu.cn; Qiaobao Zhang, zhangqiaobao@xmu.edu.cn

deposition, which significantly reduces the localized current, minimize deposition-induced dimension changes, and effectively restrain the growth of Li dendrite [33–37]. To reach uniform Li deposition, it is critical for the design and fabrication of a 3D current collector. Generally, most Li prefers to plate on the top part of the host network due to the local electric field and the shorter Li-ion diffusion pathway [38]. However, it is still a huge challenge to design a 3D Li metal host combining optimized deposition local electric filed, high conductivity, and high lithophilic active sites to acquire desired Li metal properties.

In this study, we report a composite structure that integrates the well-distributed N-doped hollow porous bowl-like hard carbon (CB) with the reduced graphene layers (CB@rGO) as a stable host for Li metal electrodes. The CBs are located in between the rGO layer to form a 3D porous, flexible film to accommodate the infinite volume changes during the Li deposition and stripping process. The CB mainly works as a short-range host framework in the local area whereas the rGO layer maintains the integrity of composite during cycling by allowing adjustment of the available space and compensating volume changes in a long-range order. In addition, the N-doped CBs offer lithophilic sites to guide Li plating and construct an electrically conductive framework with rGO to reach low local current density. With the above merits, the as-fabricated CB@rGO presents a low lithium metal nucleation overpotential of 18 mV, high CE of 98%, and stable cycling without obvious voltage fluctuation for over 600 cycles at a current density of 1 mA·cm^{-2}, which is at least comparable or even outperforming those in many previous literatures. Moreover, even at a high current density of 8 mA·cm^{-2} for the capacities of 1 mAh·cm^{-2}, a high coulombic efficiency of 96% is achieved, suggesting the advantageous structural features of CB@rGO for Li plating/stripping.

2 Experimental

2.1 Preparation of N-doped carbon bowls

Firstly, 6 mL of tetraethylorthosilicate (TEOS) was dispersed in a solution of 50 mL ethanol and 68 mL deionized water. Then, 0.4 g of resorcinol, 0.6 mL of ethylenediamine (EDA), and 0.4 mL of formaldehyde were added into the above solution under continuous magnetic stirring overnight at 30 °C. After centrifugation and collection, ammonia solution and TEOS were added to the solution in sequence. The obtained intermediates were further carbonized under an N_2 atmosphere at 800 °C for 4 h, and finally, the silica was removed by reaction with 20% HF for 24 h. After drying, N-doped CBs powder was obtained.

2.2 Preparation of CB@rGO

The N-doped CBs (20 mg) were dispersed in 50 mL deionized water, and then 0.5 mL poly (diallydimethylammonium chloride) (PDDA) was added into the solution under continuous stirring for 1 hour to get positively charged carbon bows-PDDA. Finally, the extra PDDA was removed by washing several times. Graphene oxide (GO) was prepared by the modified Hummers method reported before. The obtained carbon bows-PDDA powders were redispersed into 50 mL deionized water and added dropwise to negatively charged GO solution (24 mg GO in 500 mL deionized water) under continuous stirring to form CB@rGO. The weight and area of free-standing CB@rGO film are 3.50 mg·cm^{-2}. The free-standing CB@rGO film was obtained by vacuum freeze-drying of the sample obtained from vacuum filtering and quickly freezing after washing with deionized water 3 times. Finally, the CB@rGO film was produced by thermally annealing CB@rGO film at 700 °C for 3 h under an Ar atmosphere. For comparison, we also prepared rGO film by a similar method but without compositing of the CBs.

2.3 Materials characterization

The morphology, structure, and composition of the samples were characterized by field emission scanning electron microscopy (FE-SEM, FEI nano SEM 450), transmission electron microscopy (TEM, JEM-2100F) with energy dispersive X-ray spectrometry (EDS) elemental mapping analysis. Powder X-ray diffraction (PXRD, Philips X' Pert Pro) with Cu Kα radiation was conducted to identify the crystalline structure of samples. Raman measurements were performed on an Invia confocal Raman microscope (Horiba) using a holographic grating of 600 g·mm^{-1}. The chemical states of the samples were tested on X-ray photoelectron spectroscopy (XPS, Thermo ESCALAB 250XI) to get the fine spectra of samples. The *in-situ* TEM was performed using a TEM instrument with a 200 kV acceleration voltage by using a by using Nanofactory TEM-STM specimen holder integrated with a mobile electrical biasing probe.

2.4 Electrochemical characterization

The 2032-type coin cells were assembled in an Ar-filled glovebox to evaluate the Li plating/stripping behavior on CB@rGO, rGO, and bare Cu foil with the Li foils as the counter electrodes. The electrolyte was 1 M lithium bis (trifluoromethanesulfonyl) imide (LiTFSI) and 0.2 M $LiNO_3$ in DOL/DME (1:1, v/v, 60 μL in each coin cell). A Celgard 2400 film was acted as the separator. The electrochemical performance tests were carried out on an electrochemical test system (Land CT2001A). To test Coulombic efficiency, a fixed amount of Li was deposited on the electrode and then stripped away up to 0.5 V at various current densities.

To evaluate the performance of the CB@rGO-Li anode in a full cell, $LiFePO_4$ (Liyuan Corporation) was used as a cathode material. The $LiFePO_4$ cathode film was prepared by mixing active material, acetylene black, and polyvinylidene fluoride (PVDF) at a weight ratio of 8:1:1 in N-methylpyrrolidone. After magnetic stirring for 24 h, the slurry was coated on the aluminum current collector and dried in a vacuum oven at 120 °C for 10 h. The areal mass loading of the active materials is about 2.0 mg·cm^{-2}. To fabricate the Li-based composite electrode, the CB@rGO, rGO, and Cu were served as the anodes and Li was the counter electrode in the 2032 cell. The deposited Li-based electrodes were taken out after disassembling cells, which were denoted as CB@rGO-Li, rGO-Li, and Cu-Li, respectively. All three samples of composite electrodes have the same Li mass loading of 2 mAh·cm^{-2}. The full cells were assembled by coupling the $LiFePO_4$ and CB@rGO-Li/rGO-Li/Cu-Li as the cathodes and anodes with the above-mentioned separators and electrolyte. The electrochemical performance of the full cell was determined by cycling between 2.5 and 4.2 V at different rates from 0.1 to 10 C (1 C = 152 mA·g^{-1} based on the capacity of $LiFePO_4$).

2.5 Computational details

Ab initio molecular dynamics (AIMD) calculations are conducted under the generalized gradient approximation (GGA) using the Perdew-Burke-Ernzerhof (PBE) functionals as implemented in the Vienna *ab initio* simulation package [39]. The kinetic cutoff for plane-waves was set at 450 eV and only the gamma point was sampled. The ionic time step was set at 2 fs and the simulation was carried out in a canonical ensemble (NVT). The initial temperature of the system was set at 700 K to accelerate

the diffusion of lithium ions, and the total evolution time was set to be 20 ps. To account for the rGO layers, the oxygens suspended on the surface were taken into account in the model. The initial condition for the *ab initio* molecular dynamics simulations is that the pure lithium metal crystal is set on the left side of the rGO layers and the integrated CB and rGO electrodes, and the corresponding boundary conditions are that the rGO layers and the integrated CB and rGO electrodes are fixed during the lithium atoms diffusion. The difference between the reduced graphene nanosheets and graphene sheets was considered by taking into account the residual oxygens in the calculation, and the N-doped effect is also considered in the calculation by doping N atoms in the CB.

In the current work, the temporal and spatial evolution of Li deposition morphology during charging were captured via a nonlinear phase-field model Eq. (1) [40]

$$\frac{\partial \xi}{\partial t} = -L_\sigma\left(g'(\xi) - \kappa\nabla^2\xi\right) - L_\eta h'(\xi)\left\{\exp\left[\frac{(1-\alpha)nF\eta_\alpha}{RT}\right] - c^+\exp\left[\frac{-\alpha nF\eta_\alpha}{RT}\right]\right\} \quad (1)$$

where the phase field parameter ξ is adopted to describe two distinct phases, ξ = 0 for the electrolyte and ξ = 1 for the Li metal anode, and the values between 0 and 1 correspond to the interfacial region. $g(\xi)$ is a simple double-well function describing the two equilibrium states for the Li metal anode and the electrolyte under zero overpotential, the interpolating function $h(\xi)$ limiting the electrode reaction at the electrode-electrolyte interface. L_σ and L_η are the interface mobility and the reaction-related constant, respectively. $\eta_\alpha = \Delta\phi - E^\Theta$ and E^Θ are the activation overpotential and the standard half-cell potential, respectively. For simplicity, the movement of Li^+ concentration (c^+) was governed by Nernst-Plank Eq. (2) as

$$\frac{\partial c^+}{\partial t} = \nabla\cdot\left[D^{\text{eff}}\nabla c^+ + \frac{D^{\text{eff}}c^+}{RT}nF\nabla\phi\right] - \frac{c_s}{c_0}\frac{\partial\xi}{\partial t} \quad (2)$$

Where $D^{\text{eff}} = D^e h(\xi) + D^s(1-h(\xi))$ is the effective diffusion coefficient, D^e and D^s are the Li-ion diffusion coefficients in the electrode and the electrolyte, respectively. The source term on the right-hand side corresponds to the local accumulation/consuming rate of Li-ion due to electrochemical reactions at the electrode interface. Moreover, the electric potential (ϕ) is governed by the Poisson Eq. (3)

$$\nabla\cdot\left[\sigma^{\text{eff}}\nabla\phi\right] = I_R \quad (3)$$

where $\sigma^{\text{eff}} = \sigma^e h(\xi) + \sigma^s[1-h(\xi)]$ is the effective conductivity depending on the phase parameter, σ^e is the conductivity of the electrode, σ^s and is the conductivity of the electrolyte solution. The source term I_R is associated with charges entering/leaving due to the reaction rate at the electrode interface, having a form of $I_R = nFc_s\frac{\partial\xi}{\partial t}$. All the parameters used in the present phase field simulations are adopted from the reference [40].

3 Results and discussion

Figure 1(a) illustrates the fabrication procedure of the composite

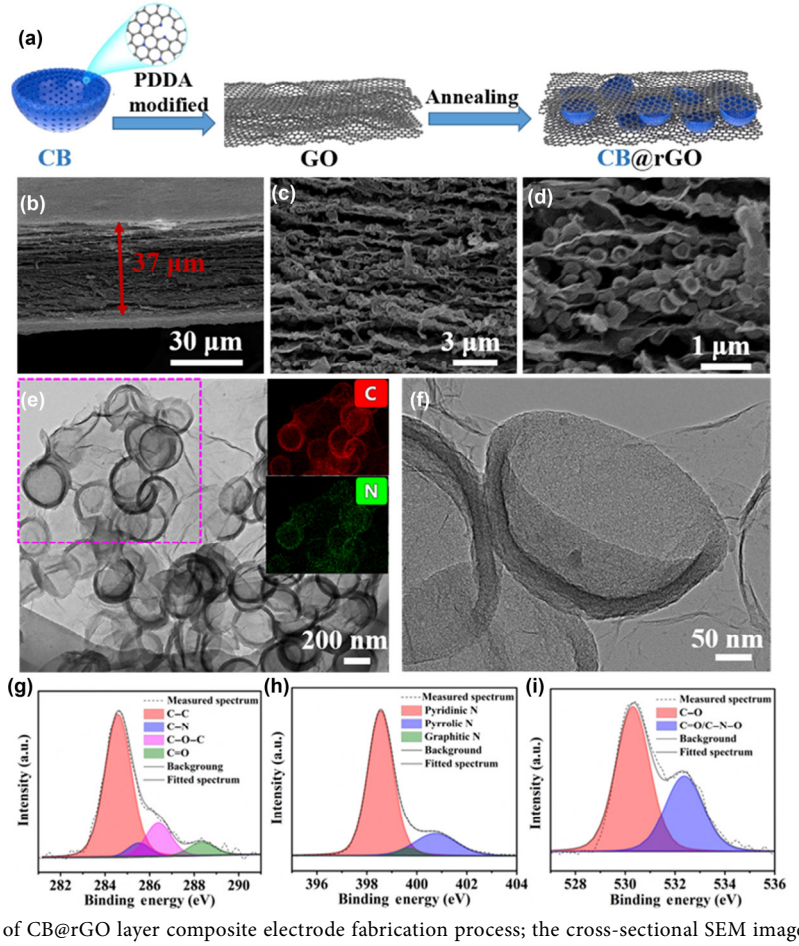

Figure 1 (a) The schematic of CB@rGO layer composite electrode fabrication process; the cross-sectional SEM images of the prepared composite electrode at (b) low and (c–d) high magnification; the TEM image of selected thin layer composite electrode at (e) low (with EDX mapping as inserted figure) and (f) high magnification; the XPS spectra of the composite electrode for the (g) C 1s, (h) N 1s and (i) O 1s peak.

electrode. First, the as-obtained N-doped CBs (Fig. S1 in the Electronic Supplementary Material (ESM)) are dispersed in poly (diallydimethylammonium chloride) (PDDA) solution under continuous stirring for 1 h to get positively charged CBs-PDDA. After that, the charged CBs-PDDA samples are washed and redispersed into the negatively charged GO solution to form CB@GO. The free-standing CB@GO film comprising of 20 mg CB and 24 mg GO is produced by vacuum filtering after washing with deionized water 3 times. Then, the final CB@rGO film is formed by thermal annealing of CB@GO under an Ar atmosphere at 700 °C for 3 h (experimental section for details is in the ESM). The comparative sample of rGO film is prepared with a similar method.

The morphology of the CB@rGO composite was characterized using SEM. The CBs are well-dispersed in the rGOs layers to form a close-packed thin film. As shown in Fig. 1(b), the total thickness of the prepared composite film electrode is around 37 μm and the maximal distance between each rGO layer could reach 1 μm. It can be clearly observed from the higher magnification SEM image (Figs. 1(c) and 1(d)) that the CBs hold up void space in the region between rGO layers. TEM characterization in Fig. 1(d) shows that CBs are well distributed between the thin rGO layers to form a thin film. Unconsolidated dispersion of each CB is important because it creates space for Li deposition at microscale. As integrated with rGO to ensure the mechanical stability of composite in macroscale, the prepared electrode has the flexibility to accommodate the large-scale volumetric change during cycling. The EDX mapping in the inserted Fig. 1(d) demonstrates a homogeneous distribution of elemental N and C components of the CBs, indicating the successful incorporation of the N element. The higher magnification TEM image (Fig. 1(f)) shows that the CB has hemispherical morphology and the wall of this carbon hemisphere has a thickness of around 20 nm. The structure of CBs and rGO composite is characterized by XRD and Raman spectroscopy. The XRD pattern (Fig. S2(a) in the ESM) of CBs has two broad peaks at 25° and 44°, which can be ascribed to the typically amorphous hard carbon. As for CB@rGO, the XRD pattern appeared to be the combination of rGO and CB (Fig. S2(b) in the ESM). Raman scattering spectroscopy shows two wide peaks at 1,360 and 1,582 cm^{-1} corresponding to the D and G bands of CBs (Fig. S3(a) in the ESM), rGO, and CB@rGO (Fig. S3(b) in the ESM). The Brunauer-Emmett-Teller (BET) surface area of CB and CB@rGO (Fig. S4 in the ESM) are measured to be 598.8 and 328.6 $m^2 \cdot g^{-1}$ by nitrogen adsorption/desorption, respectively. The chemical composition of the composite electrode surface is investigated by XPS, and the spectra are shown in Figs. 1(g)–1(i). The peaks at 284.7, 285.5, 286.5, and 288.3 eV in C 1s spectrum (Fig. 1(g)) are attributed to C–C, C–N, C–O–C, and C=O, respectively [41]. The N 1s spectrum (Fig. 1(h)) corroborates the presence of N atoms, with the peaks centered at 398.3 eV (pyridinic-N), 399.4 eV (pyrrolic-N), and 401.1 eV (graphitic-N) [42, 43]. While the peak signals of the O 1s spectrum (Fig. 1(i)) are attributed to C–O (at 530.4 eV) and C=O/C–N–O (532.7 eV) bonds [44].

The morphological changes of Li plating within the CBs and rGO composite electrode is shown along with the cross-section view of SEM images in Figs. 2(a)–2(c). The Li plating was

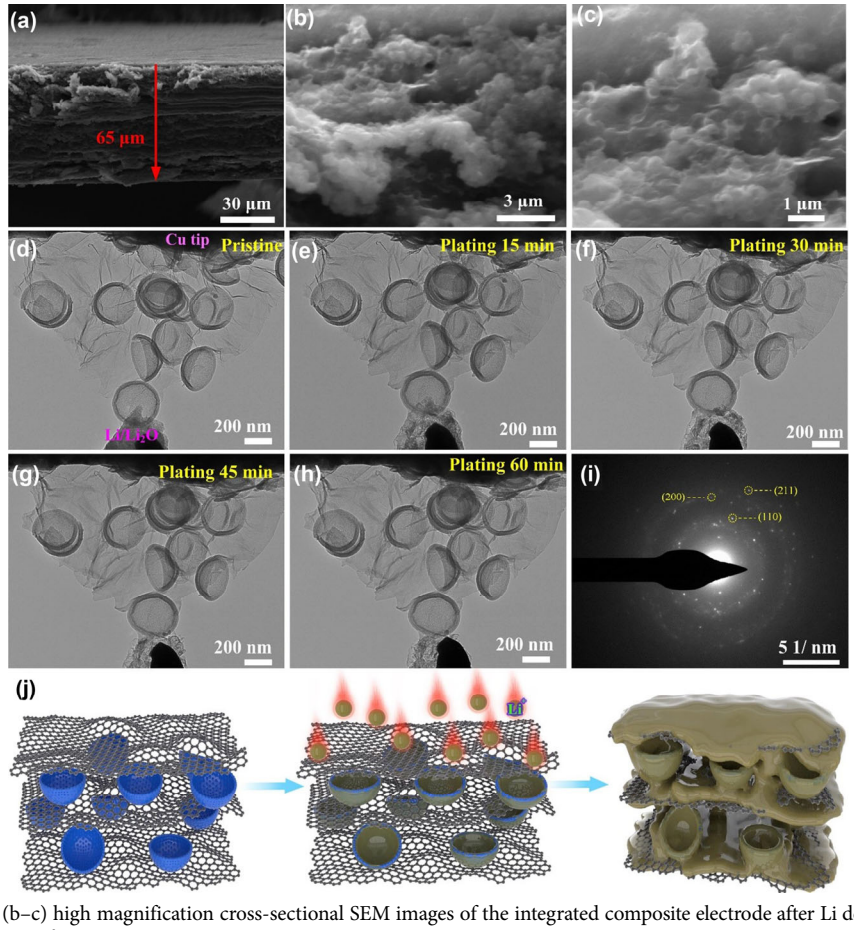

Figure 2 (a) The low and (b–c) high magnification cross-sectional SEM images of the integrated composite electrode after Li deposition for 1 $mAh \cdot cm^{-2}$ at the current density of 1 $mA \cdot cm^{-2}$; the selected TEM images of *in situ* Li/integrated composite electrode (d) at pristine state, (e) after 15 min, (f) 30 min, (g) 45 min and (h) 60 min Li plating; (i) The SAED pattern of the CB@rGO composite electrode filled up with Li, after Li plating for 60 min; (j) the schematic illustration of the mechanisms underlying the Li deposition behavior on the integrated composite electrode.

processed in the coin cell by using the electrolyte of 1 M LiTFSI in 1,3-dioxolane (DOL)/1 and 2-dimethoxyethane (DME) (1:1 volume ratio) with 2 wt.% $LiNO_3$ as the additive. As shown in Fig. 2(a), the thickness of the composite electrode reaches 65 μm after Li plating with a capacity of 1 mAh·cm^{-2} at the current of 1 mA·cm^{-2}, and the Li plating is mainly stored inside the integrated composite electrode rather than on the surface. The high magnification SEM images in Figs. 2(b) and 2(c) show that the deposited Li is closely bound to both CBs and rGO layer and has full filled the inter-layer void space held up by the CBs, indicating that the fabricated structure could successfully guide a homogeneously Li deposition. When the current density was up to 5 mA·cm^{-2}, as shown in Figs. S5(a) and S5(b) in the ESM, the Li was also uniformly stored inside the integrated composite electrode and the surface of the CB@rGO is smooth. In contrast, Li tended to nucleate locally to form Li metal on the rGO film and obvious protuberances are observed (Fig. S5(c) in the ESM). The cross-sectional SEM image even shows that Li is mainly stored onto the top surface of the rGO scaffold (Fig. S5(d) in the ESM). To demonstrate the live Li plating track and the structural evolution in the composite material, *in-situ* TEM characterization through a nano battery configuration has been conducted [45–47]. The evolution process was recorded as shown in Movie ESM1, and the selected real-time image is shown in Figs. 2(d)–2(h). The CB@rGO, Li metal, and naturally grown Li_2O layer are set as the working electrode, the counter electrode, and the solid electrolyte of the nano battery, respectively. The CB@rGO is attached to a copper tip, and then transferred into the TEM-scanning tunneling microscope (STM) specimen holder. The Li metal with a thin Li_2O layer is loaded onto a movable tungsten tip in a glove box and then transferred into the TEM instrument (JEOL-2100). The Li-ions go through the Li_2O layer to deposition on the CB@rGO working electrode under applied voltages of –3 V. According to the *in-situ* TEM images, the Li metal prefers to nucleate in the inner-wall of the CB and then fill the CB (Fig. 2(e)). After that, the Li slowly plated uniformly along with the rGO layer to the region close to the current collector (Cu tip), and only slightly morphological evolution was caused during the Li plating process and no Li dendrite growth was observed, indicating the advantageous structural features of CB@rGO for Li plating (Figs. 2(d)–2(h)). Figure 2(i) presents the selected area electron diffraction pattern (SAED) of Li-filled CB@rGO working electrode after Li plating for 60 min, which exhibits several separate diffraction spots (marked with the yellow circles) superimposed on diffraction rings and can be indexed as metallic Li [48], suggesting the successful deposition of Li on CB@rGO composite. The corresponding nucleation and plating mechanism of metallic Li on CB@rGO is described in Fig. 2(j). The CB in the rGO layer with N-doping and the sharp curves, which is full of lithiophilic functional groups and negativity of surface charge, offering a multitude of uniform nucleation sites and space for the high-efficient and homogeneous Li deposition. The deposited Li tends to nucleate uniformly at the CBs first due to the low binding energy of metallic Li with the pyridinic-N, pyrrolic-N, or graphitic-N functional groups [49, 50]. Afterwards, as Li deposition continues, it grows along the perpendicular axes in the plane due to the high specific surface area. By contrast, when employing the rGO layer without CB (Fig. S4(e) in the ESM) and Cu foil as hosts, the nucleation sites of Li are isolated and randomly distributed because of the rough and lithiophobic surface. To further disclose the underlying mechanisms of the Li deposition behavior, the molecular dynamic evolution snapshots at the selected simulation time of GO and CB@rGO are simulated via molecular dynamic evolution snapshots.

To understand the dynamic process of Li intercalation and lithiation mechanism, AIMD simulations are conducted [51]. As shown in Figs. 3(a) and 3(b), immediately after the onset of stimulation, the Li^+ ions started to intercalate into the rGO layers and the CB with rGO layer composite. Comparing with the diffusion behavior of Li in rGO layers, Li in the CB with rGO layer composite is additionally coupled with the

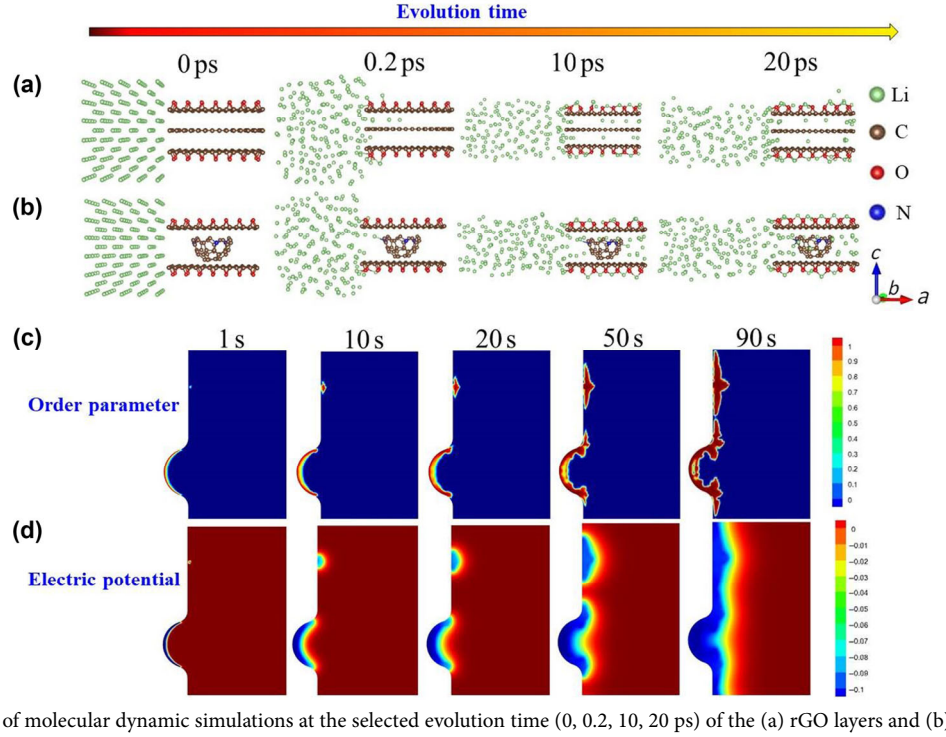

Figure 3 Snapshots of molecular dynamic simulations at the selected evolution time (0, 0.2, 10, 20 ps) of the (a) rGO layers and (b) integrated CB@rGO electrodes. Phase-field simulation results of (c) the local Li deposition morphology and (d) the electric potential at different evolution times t (1, 10, 20, 50, 90 s).

adsorption process. With the evolution time increase, the Li atoms accumulate in the CB composite much more than in the rGO layers, which indicates the N doped CB has a more powerful Li storage capacity. The underlying mechanism of this unique Li growth manner is further explained via a nonlinear phase-field model [40]. The local Li deposition morphology and the electric potential at different evolution time t (1, 10, 20, 50, 90 s) are shown in Figs. 3(c) and 3(d), respectively. Differing from the conventional growth of flat-field lithium dendrites, the curved model of CB has more advantages. Firstly, a void space in the curved field provides expanded volume for Li deposition; secondly, the traditional Li dendrites grow towards the counter electrode directly and pierce the diaphragm causing a short circuit, whereas the curved field changes the growth direction of Li dendrites to a certain extent, and Li will grow toward the center of the sphere in the curved field. Finally, during the platting, Li ions are deposited within the CBs and remain confined due to the bowl shape, which prevents Li dendrite growth and alleviates the short circuit problem.

Coulombic efficiency (CE) is a key parameter to evaluate the sustainability and practicality of the specific electrode for the Li battery. The three-electrode cells (Li vs. CB@rGO, rGO or bare Cu foil) with an electrolyte of 1 M LiTFSI in DOL/DME (1:1 volume ratio) with 2 wt.% $LiNO_3$ as the additive are assembled to characterize the reversibility of CB@rGO host, rGO host, and Cu foil for the Li plating/stripping CE at different current densities are given in Fig. 4. Figure 4(a) shows the Li deposition electrochemical behaviors at a current density of 1.0 mA·cm^{-2} with a cycling capacity of 1 mAh·cm^{-2}. The CE of CB@rGO increases gradually in the initial cycles and then stabilizes at above 98% for over 600 cycles. Although rGO and

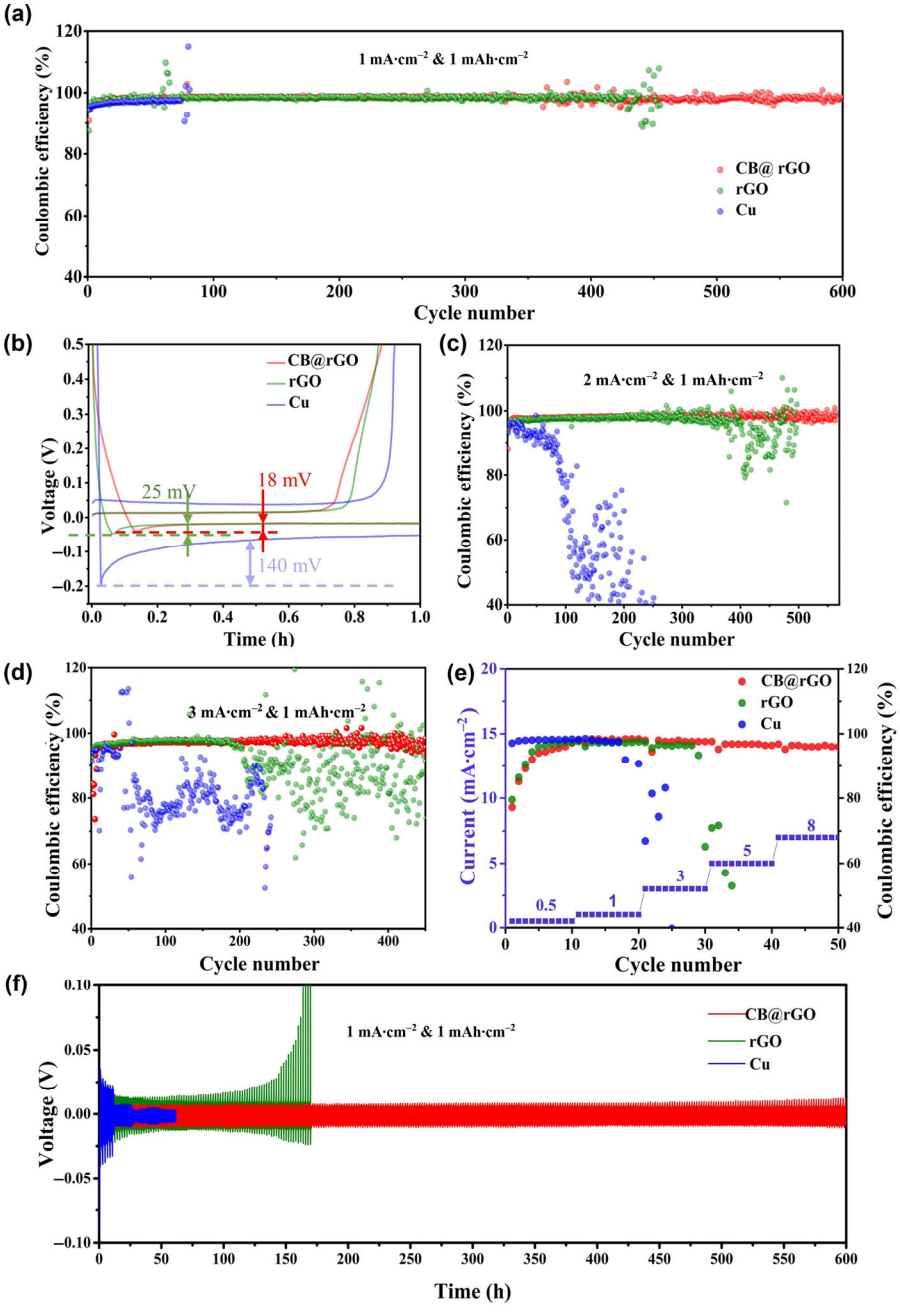

Figure 4 (a) The Coulombic efficiency and (b) voltage profiles of CB@rGO, rGO host, and bare Cu foil with a cycling capacity of 1 mAh·cm^{-2} at a current density of 1 mA·cm^{-2}. The Coulombic efficiency of CB@rGO, rGO host, and bare Cu foil with a cycling capacity of 1 mAh·cm^{-2} at a current density of (c) 2 mA·cm^{-2}, (d) 3 mA·cm^{-2}, and at different current densities of (e) 0.5 to 8 mA·cm^{-2}, respectively. (f) Galvanostatic cycling of symmetrical Li-CB@rGO, Li-rGO, and Li-Cu cells at a current density of 1 mA·cm^{-2}.

Cu show a stable CE after the first several cycles, it fluctuates randomly after 400 and 80 cycles, respectively, possibly due to the short circuit caused by Li dendrites. The CE can maintain at a stable value without obvious fluctuation, suggesting that the CB@rGO composite can provide a stable interface feature with lithophilic groups and a steady host structure accommodating the volume changes. The 1st cycle voltage profiles in Fig. 4(b) show that there are obvious overpotentials of 0.14, 0.025, 0.018 V for bare Cu foil, rGO, and CB@rGO, implying that the nucleation and plating of Li on Cu require higher binding energy compare to CB@rGO or rGO composite electrode. Since the CB@rGO or rGO host has a large surface area that needs to be fully passivated by the SEI layer before the Li nucleation and plating process, a short slop can be observed at the beginning of the electrochemical process.

As current density increased, the CB@rGO host shows an obvious superiority. Figures 4(c) and 4(d) show the Coulombic efficiency of CB@rGO, rGO host, and bare Cu foil with a cycling capacity of 1 mAh·cm^{-2} at a current of 2 and 3 mA·cm^{-2}, respectively. The bare Cu foil-based cell is unable to reach a stable cycle due to uncontrolled dendritic growth at a high current rate. For the rGO electrode, the performance is better than the Cu electrode as the result of a reduction in localized current density due to the large surface area. However, the closed packed structure and lithiophobic surface lead to Li plating agglomerate on the top surface of the rGO electrode. Therefore, rGO electrode is hard to stand for a long cycle life at a high current rate. The CB@rGO composite electrode shows quite impressive behavior, especially at 3 mA·cm^{-2}, around two times longer stable cycling achieved compare to the rGO electrode. After 100 charge/discharge cycles (Fig. S6 in the ESM), the CB@rGO electrode exhibits a very intact structure, whereas the rGO film appears to be broken. The Coulombic efficiencies of Li plating/stripping of CB@rGO, rGO host, and bare Cu foil at different current densities are shown in Fig. 4(e). The Coulombic efficiency of CB@rGO increases gradually in the initial cycles and then stabilizes at above 98.4% at a current density of 1 mA·cm^{-2}, and shows a high Coulombic efficiency of 96% even at a high current density of 8 mA·cm^{-2} for the capacities of 1 mAh·cm^{-2}. In contrast, the half-cells with the rGO and bare Cu foil electrodes fail at a current density of 3 and 1 mA·cm^{-2}, respectively, owing to the short-circuiting caused by the Li dendrites. We compared the CE performances of the previously reported results of other Li metal scaffolds with our work (Table S1 in the ESM), which demonstrates that our results are at least comparable or even better than those in published articles. The galvanostatic cycling stability of the Li-CB@rGO, Li-rGO and Li-Cu anodes are tested in cells with the Li foils as the counter electrodes. The Li-CB@rGO, Li-rGO and Li-Cu electrodes are prepared by pre-electroplating Li on the CB@rGO and bare Cu with a capacity of 2 mAh·cm^{-2} at a current density of 0.5 mA·cm^{-2}. As shown in Fig. 4(f), the voltage hysteresis of the cell with Li-rGO electrode gradually increases and the cell shows an ultra-large polarization after 150 h owing to the Li densities and dead Li. While the voltage hysteresis of the cell with Li-Cu electrode gets short circuit after 15 h because of the Li densities. In the cell with Li-CB@rGO electrode, the voltage hysteresis is smaller and remains stable for 600 h, indicating better plating/stripping stability than Li-rGO and Li-Cu. The outstanding electrochemical performance of the CB@rGO host is contributed by its special structure and composition can sufficiently prohibit the Li dendrite formation, efficiently eliminate Li plating at the specific area of the 3D host, and preferably accommodate on infinite relative volume change.

To further verify these remarkable properties and the performance of the CB@rGO host for practical application, the pre-lithiated CB@rGO host, rGO host or bare Cu foil electrodes are assembled into full cell employing the $LiFePO_4$ (LFP) electrode as the cathodes. The Li plating process is carried out in coin-type 2032 cell with Li metal foil as the counter electrodes and the host, rGO host, or bare Cu foil served as the working electrode. The specific capacity of the full cell is based on mass of the cathode. The amount of deposited Li of all three samples (denoted as Li-CB@rGO, Li-rGO, and Li-Cu) is 2 mAh·cm^{-2} accomplished by 4h deposition at a current density of 0.5 mA·cm^{-2}. The rate capability and cycling stability of assembled coin cell are shown in Fig. 5(a). All these three cells could deliver a capacity of 148 mAh·g^{-1} at 0.1 C (1 C = 152 mA·g^{-1} based on the LFP cathode) without any voltage differences for the first cycle (shown in Fig. 5(b)). As the current density continues increasing, the cell consistently exhibits a much better rate

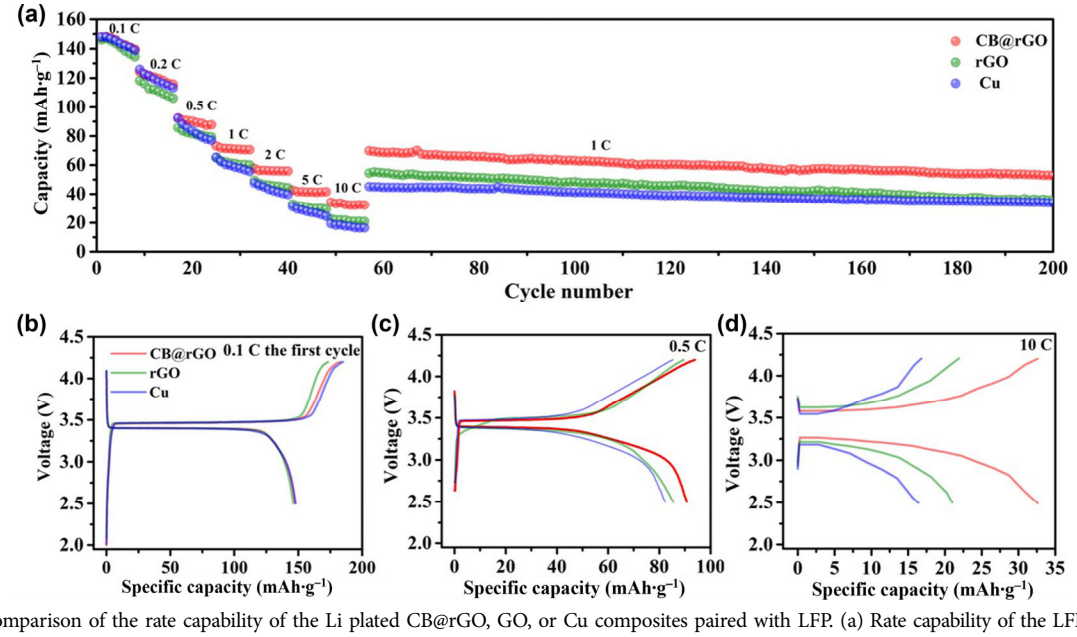

Figure 5 Comparison of the rate capability of the Li plated CB@rGO, GO, or Cu composites paired with LFP. (a) Rate capability of the LFP/Li-CB@rGO, LFP/Li-rGO and LFP/Li-Cu cells at different rates from 0.1 C–10 C; Galvanostatic profiles of LFP/Li-CB@rGO, LFP/Li-rGO and LFP/Li-Cu cells full-cells at current rates of (b) 0.1 C , (c) 0.5 C and (d) 10 C (1 C = 152 mA·g^{-1}).

capability than these of Li-rGO /LFP and Li-Cu/LFP. A much higher capacity is achieved with Li plated CB@rGO composite anodes in the rate profile. The voltage profiles shown in Fig. 5(c) reveal that the advantages of the pre-lithiated CB@rGO composite are already quite obvious when the cells are charged and discharged at 0.5 C. The discharge capacity of cells assembled with Li plated CB@rGO composite could reach 90.6 mAh·g^{-1}, whereas the cells paired with Li plated rGO or Cu could only achieve a discharged capacity of 83.7 and 80.4 mAh·g^{-1}, respectively. Besides, the delivered capacity is better maintained for the full cell assembled with pre-lithiated CB@rGO composite electrode. A more pronounced difference appeared when the current density was further increased. When the current approaches 10C, a much higher LFP capacity (33 mAh·g^{-1}) is achieved with pre-lithiated CB@rGO composite. In comparison, the cell assembled with pre-lithiated rGO or Cu foil can only offer a capacity of 20.7 and 16.7 mAh·g^{-1}, respectively. Moreover, the voltage profiles shown in Fig. 5(d) demonstrate a much lower overpotential extent of the CB@rGO based cell. Therefore, the cell paired with a pre-lithiated CB@rGO composite electrode could achieve a high energy density and power density as well, which benefits its practical application.

4 Conclusions

In summary, we designed a 3D porous film electrode with specific morphology and chemical properties to stabilize the Li metal anode by well-distributed CB in between the rGO layers. It is demonstrated that this novel structure has excellent electrical conductivity and porous 3D structure that can effectively guide Li growth, accommodate the deposited Li metal, and alleviate the severe volume change during the Li deposition/dissolution process, as confirmed by *in-situ* TEM and *ex-situ* SEM observations. The CB mainly works as a short-range host framework in the local area whereas the rGO layer maintains the integrity of the composite to adjust the space change in long-range order during cycling. By confining Li inside the CB@rGO host, the formation of Li dendrites is eliminated. Our study not only provides a good CB@rGO-host and pre-lithiated CB@rGO composite anode electrode, but also paves a path to a novel 3D electrode design for those active materials suffering from severe volume expansion.

Acknowledgements

This work is supported by the National Natural Science Foundation of China (Nos. 52072323 and 51872098) and the "Double-First Class" Foundation of Materials and Intelligent Manufacturing Discipline of Xiamen University, as well as Postdoctoral Foundation of China (2018M632929).

Electronic Supplementary Material: Supplementary material (further details of SEM imaging and Raman spectroscopy measurements, BET test, 1 table and *in-situ* TEM video) is available in the online version of this article at https://doi.org/10.1007/s12274-021-3482-0.

References

[1] Liang, Y.; Zhao, C. Z.; Yuan, H; Chen, Y.; Zhang, W.; Huang, J. Q.; Yu D.; Liu, Y; Titirici, M. M.; Chueh, Y. L. et al. A review of rechargeable batteries for portable electronic devices. *InfoMat.* **2019**, *1*, 6–32.

[2] Wang, A. X.; Zhang, X. Y.; Yang, Y. W.; Huang, J. X.; Liu, X. J.; Luo, J. Y. Horizontal centripetal plating in the patterned voids of Li/graphene composites for stable lithium-metal anodes. *Chem* **2018**, *4*, 2192–2200.

[3] Wu, M.; Li, Y.; Liu, X.; Yang, S.; Ma, J.; Dou, S. Perspective on solid-electrolyte interphase regulation for lithium metal batteries. *SmartMat.* **2020**, *2*, 5–11.

[4] Pu, K. C.; Zhang, X.; Qu, X. L.; Hu, J. J.; Li, H. W.; Gao, M. X.; Pan, H. G.; Liu, Y. F. Recently developed strategies to restrain dendrite growth of Li metal anodes for rechargeable batteries. *Rare Met.* **2020**, *39*, 616–635.

[5] Winter, M.; Barnett, B.; Xu, K. Before Li ion batteries. *Chem. Rev.* **2018**, *118*, 11433–11456.

[6] Xu, W.; Wang, J. L.; Ding, F.; Chen, X. L.; Nasybulin, E.; Zhang, Y. H.; Zhang, J. G. Lithium metal anodes for rechargeable batteries. *Energy Environ. Sci.* **2014**, *7*, 513–537.

[7] Cheng, X. B.; Zhang, R.; Zhao, C. Z.; Zhang, Q. Toward safe lithium metal anode in rechargeable batteries: A review. *Chem. Rev.* **2017**, *117*, 10403–10473.

[8] Zhang, K.; Lee, G. H.; Park, M.; Li, W. J.; Kang, Y. M. Recent developments of the lithium metal anode for rechargeable non-aqueous batteries. *Adv. Energy Mater.* **2016**, *6*, 1600811.

[9] Zhamu, A.; Chen, G. R.; Liu, C. G.; Neff, D.; Fang, Q.; Yu, Z. N.; Xiong, W.; Wang, Y. B.; Wang, X. Q.; Jang, B. Z. Reviving rechargeable lithium metal batteries: Enabling next-generation high-energy and high-power cells. *Energy Environ. Sci.* **2012**, *5*, 5701–5707.

[10] Chen, X. R.; Zhao, B. C.; Yan, C.; Zhang, Q. Review on Li deposition in working batteries: From nucleation to early growth. *Adv. Mater.* **2021**, *33*, 2004128.

[11] Chen, X. R.; Yao, Y. X.; Yan, C.; Zhang, R.; Cheng, X. B.; Zhang, Q. A diffusion-reaction competition mechanism to tailor lithium deposition for lithium-metal batteries. *Angew. Chem., Int. Ed.* **2020**, *59*, 7743–7747.

[12] Cheng, X. B.; Zhang, R.; Zhao, C. Z.; Wei, F.; Zhang, J. G.; Zhang, Q. A review of solid electrolyte interphases on lithium metal anode. *Adv. Sci.* **2016**, *3*, 1500213.

[13] Xu, R.; Zhang, X. Q.; Cheng, X. B.; Peng, H. J.; Zhao, C. Z.; Yan, C.; Huang, J. Q. Artificial soft-rigid protective layer for dendrite-free lithium metal anode. *Adv. Funct. Mater.* **2018**, *28*, 1705838.

[14] Chi, S. S.; Liu, Y. C.; Song, W. L.; Fan, L. Z.; Zhang, Q. Prestoring lithium into stable 3D nickel foam host as dendrite-free lithium metal anode. *Adv. Funct. Mater.* **2017**, *27*, 1700348.

[15] Xu, K. Electrolytes and interphases in Li-ion batteries and beyond. *Chem. Rev.* **2014**, *114*, 11503–11618.

[16] Cao, X.; Ren, X. D.; Zou, L. F.; Engelhard, M. H.; Huang, W.; Wang, H.; Matthews, B. E.; Lee, H.; Niu, C. J.; Arey, B. W. et al. Monolithic solid-electrolyte interphases formed in fluorinated orthoformate-based electrolytes minimize Li depletion and pulverization. *Nat. Energy* **2019**, *4*, 796–805.

[17] Ding, F.; Xu, W.; Graff, G. L.; Zhang, J.; Sushko, M. L.; Chen, X. L.; Shao, Y. Y.; Engelhard, M. H.; Nie, Z. M.; Xiao, J. et al. Dendrite-free lithium deposition via self-healing electrostatic shield mechanism. *J. Am. Chem. Soc.* **2013**, *135*, 4450–4456.

[18] Wang, D. D.; Liu, H. D.; Li, M. Q.; Xia, D. W.; Holoubek, J.; Deng, Z.; Yu, M. Y.; Tian, J. H.; Shan, Z. Q.; Ong, S. P. et al. A long-lasting dual-function electrolyte additive for stable lithium metal batteries. *Nano Energy* **2020**, *75*, 104889.

[19] Liu, H. D.; Holoubek, J.; Zhou, H. Y.; Chen, A.; Chang, N.; Wu, Z. H.; Yu, S. C.; Yan, Q. Z.; Xing, X.; Li, Y. J. et al. Ultrahigh coulombic efficiency electrolyte enables Li||span batteries with superior cycling performance. *Mater. Today* **2020**, *42*, 17–28.

[20] Liu, H. D.; Zhou, H. Y.; Lee, B. S.; Xing, X.; Gonzalez, M.; Liu, P. Suppressing lithium dendrite growth with a single-component coating. *ACS Appl. Mater. Interfaces* **2017**, *9*, 30635–30642.

[21] Gao, Y.; Yan, Z. F.; Gray, J. L.; He, X.; Wang, D. W.; Chen, T. H.; Huang, Q. Q.; Li, Y. C.; Wang, H. Y.; Kim, S. H. et al. Polymer-inorganic solid-electrolyte interphase for stable lithium metal batteries under lean electrolyte conditions. *Nat. Energy* **2019**, *18*, 384–389.

[22] Liu, Q. C.; Xu, J. J.; Yuan, S.; Chang, Z. W.; Xu, D.; Yin, Y. B.; Li, L.; Zhong, H. X.; Jiang, Y. S.; Yan, J. M. et al. Artificial protection film on lithium metal anode toward long-cycle-life lithium-oxygen batteries. *Adv. Mater.* **2015**, *27*, 5241–5247.

[23] Zhou, H. Y.; Yu, S. C.; Liu, H. D.; Liu, P. Protective coatings for lithium metal anodes: Recent progress and future perspectives. *J. Power Sources* **2020**, *450*, 227632.

[24] Liu, H. D.; Yue, X. J.; Xing, X.; Yan, Q. Z.; Huang, J.; Petrova, V.;

Zhou, H. Y.; Liu, P. A scalable 3D lithium metal anode. *Energy Storage Mater*. **2019**, *16*, 505–511.
[25] Li, H. P.; Ji, X. Y.; Liang, J. J. Dual-functional ion redistributor for dendrite-free lithium metal anodes. *Rare Met*. **2020**, *39*, 861–862.
[26] Shi, H. D.; Li, Y. G.; Lu, P. F.; Wu, Z. S. Single-atom cobalt coordinated to oxygen sites on graphene for stable lithium metal anodes. *Acta Phys.–Chim. Sin*. **2021**, *37*, 2008033.
[27] Huang, X.; Feng, X. Y.; Zhang, B.; Zhang, L.; Zhang, S. C.; Gao, B.; Chu, P. K.; Huo, K. F. Lithiated $NiCo_2O_4$ nanorods anchored on 3D nickel foam enable homogeneous Li plating/stripping for high-power dendrite-free lithium metal anode. *ACS Appl. Mater. Interfaces* **2019**, *11*, 31824–31831.
[28] Liu, K.; Pei, A.; Lee, H. R.; Kong, B.; Liu, N.; Lin, D. C.; Liu, Y. Y.; Liu, C.; Hsu, P. C.; Bao, Z. N. et al. Lithium metal anodes with an adaptive "solid-liquid" interfacial protective layer. *J. Am. Chem. Soc*. **2017**, *139*, 4815–4820.
[29] Sun, Y. M.; Zheng, G. Y.; Seh, Z. W.; Liu, N.; Wang, S.; Sun, J.; Lee, H. R.; Cui, Y. Graphite-encapsulated Li-metal hybrid anodes for high-capacity Li batteries. *Chem* **2016**, *1*, 287–297.
[30] Zheng, G. Y.; Lee, S. W.; Liang, Z.; Lee, H. W.; Yan, K.; Yao, H. B.; Wang, H. T.; Li, W. Y.; Chu, S.; Cui, Y. Interconnected hollow carbon nanospheres for stable lithium metal anodes. *Nat. Nanotechnol*. **2014**, *9*, 618–623.
[31] Liu, S. F.; Xia, X. H.; Zhong, Y.; Deng, S. J.; Yao, Z. J.; Zhang, L. Y.; Cheng, X. B.; Wang, X. L.; Zhang, Q.; Tu, J. P. 3D TiC/C core/shell nanowire skeleton for dendrite-free and long-life lithium metal anode. *Adv. Energy Mater*. **2018**, *8*, 1702322.
[32] Zhao, Q.; Hao, X. G.; Su, S. M.; Ma, J. B.; Hu, Y.; Liu, Y.; Kang, F. Y.; He, Y. B. Expanded-graphite embedded in lithium metal as dendrite-free anode of lithium metal batteries. *J. Mater. Chem. A* **2019**, *7*, 15871–15879.
[33] Zheng, Z. M.; Wu, H. H.; Liu, H. D.; Zhang, Q. B.; He, X.; Yu, S. C.; Petrova, V.; Feng, J.; Kostecki, R.; Liu, P. et al. Achieving fast and durable lithium storage through amorphous FeP nanoparticles encapsulated in ultrathin 3D P-doped porous carbon nanosheets. *ACS Nano* **2020**, *14*, 9545–9561.
[34] Zhang, R.; Shen, X.; Cheng, X. B.; Zhang, Q. The dendrite growth in 3D structured lithium metal anodes: Electron or ion transfer limitation? *Energy Storage Mater*. **2019**, *23*, 556–565.
[35] Shi, P.; Li, T.; Zhang, R.; Shen, X.; Cheng, X. B.; Xu, R.; Huang, J. Q.; Chen, X. R.; Liu, H.; Zhang, Q. Lithiophilic LiC_6 layers on carbon hosts enabling stable Li metal anode in working batteries. *Adv. Mater*. **2019**, *31*, 1807131.
[36] Zhao, H.; Lei, D. N.; He, Y. B.; Yuan, Y. F.; Yun, Q. B.; Ni, B.; Lv, W.; Li, B. H.; Yang, Q. H.; Kang, F. Y. et al. Compact 3D copper with uniform porous structure derived by electrochemical dealloying as dendrite-free lithium metal anode current collector. *Adv. Energy Mater*. **2018**, *8*, 1800266.
[37] Yun, Q. B.; He, Y. B; Lv, W.; Zhao, Y.; Li, B. H.; Kang, F. Y.; Yang, Q. H. Chemical dealloying derived 3D porous current collector for Li metal anodes. *Adv. Mater*. **2016**, *28*, 6932–6939.
[38] Lu, L. L.; Ge, J.; Yang, J. N.; Chen, S. M.; Yao, H. B.; Zhou, F.; Yu, S. H. Free-standing copper nanowire network current collector for improving lithium anode performance. *Nano Lett*. **2016**, *16*, 4431–4437.
[39] Kresse, G.; Furthmüller, J. Efficient iterative schemes for *ab initio* total-energy calculations using a plane-wave basis set. *Phys. Rev. B: Condens. Matter Mater. Phys*. **1996**, *54*, 11169.
[40] Zhang, H.; Liu, Z.; Liang, L.; Chen, L.; Qi, Y.; Harris, S. J.; Lu, P.; Chen, L. Understanding and predicting the lithium dendrite formation in Li-ion batteries: Phase field model. *ECS Transactions* **2014**, *61*, 1.
[41] Nan, Y.; Li, S. M.; Shi, Y. Z.; Yang, S. B.; Li, B. Gradient-distributed nucleation seeds on conductive host for a dendrite-free and high-rate lithium metal anode. *Small* **2019**,*15*, 1903520.
[42] Sharifi, T.; Hu, G.; Jia, X. E.; Wagberg, T. Formation of active sites for oxygen reduction reactions by transformation of nitrogen functionalities in nitrogen-doped carbon nanotubes. *ACS Nano* **2012**, *6*, 8904–8912.
[43] Rabchinskii, M. K.; Ryzhkov, S. A.; Kirilenko, D. A.; Ulin, N. V.; Baidakova, M. V.; Shnitov, V. V.; Pavlov, S. I.; Chumakov, R. G.; Stolyarova, D. Y.; Besedina, N. A. et al. From graphene oxide towards aminated graphene: Facile synthesis, its structure and electronic properties. *Sci. Rep*. **2020**, *10*, 1–12.
[44] Zhang, J.; Li, C. Q.; Peng, Z. K.; Liu, Y. S.; Zhang, J. M.; Liu, Z. Y.; Li, D. 3D free-standing nitrogen-doped reduced graphene oxide aerogel as anode material for sodium ion batteries with enhanced sodium storage. *Sci. Rep*. **2017**, *7*, 1–7.
[45] Zhang, Q.; Chen, H.; Luo, L.; Zhao, B.; Luo, H.; Han, X.; Wang, J.; Wang, C.; Yang, Y.; Zhu, T.; Liu, M. Harnessing the concurrent reaction dynamics in active Si and Ge to achieve high performance lithium-ion batteries. *Energy Environ. Sci*. **2018**, *11*, 669–681.
[46] Cheng, Y.; Zhang, L.; Zhang, Q.; Li, J.; Tang, Y.; Delmas, C.; Zhu, T.; Winter, M.; Wang, M.; Huang, J. Understanding all solid-state lithium batteries through in situ transmission electron microscopy. *Mater. Today* **2020**, *42*, 137–161.
[47] Li, Y.; Zhang, Q.; Yuan, Y.; Liu, H.; Yang, C.; Lin, Z.; Lu, J. Surface amorphization of vanadium dioxide (B) for K-ion battery. *Adv. Energy Mater*. **2020**, *10*, 2000717.
[48] Liu, S.; Wang, A.; Li, Q.; Wu, J.; Chiou, K.; Huang, J.; Luo, J. Crumpled graphene balls stabilized dendrite-free lithium metal anodes. *Joule* **2018**, *2*, 184–193.
[49] Zhang, C.; Liu, S.; Li, G.; Zhang, C.; Liu, X.; Luo, J. Incorporating ionic paths into 3D conducting scaffolds for high volumetric and areal capacity, high rate lithium-metal anodes. *Adv. Mater*. **2018**, *30*, 1801328.
[50] He, X.; Yang, Y.; Cristian, M. S.; Wang, J.; Hou, X.; Yan, B.; Li, J.; Zhang, T.; Paillard, E.; Swietoslawski, M. et al. Uniform lithium electrodeposition for stable lithium-metal batteries. *Nano Energy* **2020**, *67*, 104172.
[51] Zhao, L.; Wu, H. H.; Yang, C.; Zhang, Q.; Zhong, G.; Zheng, Z.; Chen, H.; Wang, J.; He, K.; Wang, B. et al. Mechanistic origin of the high performance of yolk@shell Bi_2S_3@N-doped carbon nanowire electrodes. *ACS Nano* **2018**, *12*, 12597–12611.